July 2026
Volume 2
Issue 3

DOI: 10.48308/ijce.2026.247519.1036

Interdisciplinary Journal of Civil Engineering
Shahid Beheshti University

A Conservation-Oriented Seismic Assessment and Targeted CFRP Strengthening Strategy for Sib Castle, Iran

Authors:

Mehdi Shahraki[1], *, Amin Fakouri-Nejad[1]

Abstract

Historic adobe monuments are vulnerable to seismic cracking, yet retrofit studies rarely address irregular three-dimensional geometry alongside conservation constraints. This study assessed Sib Castle, Iran, using a nonlinear Abaqus macro-model with Concrete Damaged Plasticity to identify critical regions and compare targeted grid and diagonal carbon-fiber-reinforced polymer (CFRP) layouts. Model response was checked against an adobe wall tested under in-plane cyclic loading; the experimental first loading branch and numerical pushover differed by 1.55% in integrated force–displacement area. Three pairs of horizontal ground motions (Tabas, Kobe and Sarpol-e Zahab), scaled with reference to Iranian Standard 2800, were applied in nonlinear response-history analyses. In the unstraightened castle, tensile demand concentrated around openings, wall intersections and roof interfaces. Under the Tabas record, peak principal tensile stress decreased from 5.26 MPa to 0.191 MPa with grid strengthening and 0.193 MPa with diagonal strengthening. First-story X-direction relative displacement decreased from 22 cm to 5 cm and 19 cm, respectively, representing reductions of 77.3% and 13.6%. The grid layout performed better in this direction, although improvements were not uniform across directions. These findings support targeted CFRP intervention while acknowledging the idealized bonded interface.

Keywords: Adobe Masonry, Seismic Assessment, Finite-Element Modelling, CFRP, Heritage Conservation

1. Department of Civil Engineering, ZAH. C., Islamic Azad University, Zahedan, Iran

*Corresponding Author: Mehdi.shahraki@iau.ac.ir

1. Introduction

Historic earthen buildings preserve construction traditions that are difficult to reproduce once lost. Their seismic weakness arises from low masonry tensile resistance, substantial mass and the limited capacity of earthen joints to accommodate cyclic opening and sliding. At the scale of a fortress, vertical setbacks, openings, intersecting walls and timber–earth roof connections can concentrate in-plane shear and out-of-plane deformation. Both the local wall mechanism and the overall three-dimensional load path must therefore be considered (Mirjalili et al., 2020; Castellazzi et al., 2017).

Strengthening historic adobe presents a structural and conservation problem at the same time. Heavy jackets may introduce additional mass and modify the response of the original walls. Externally bonded fiber-reinforced polymer (FRP) strips offer tensile reinforcement at limited weight, but their benefits depend on substrate strength, anchorage, moisture and the extent of historic surface affected. Conservation guidance favors the least intervention consistent with an explicitly diagnosed structural deficiency (ICOMOS, 2003; Valluzzi et al., 2014; Petrovčič & Kilar, 2022).

Nonlinear finite-element modelling provides a practical means of exploring the response of a geometrically irregular monument without destructive testing. The modelling objective is not to reproduce every mortar joint. It is to capture the principal redistribution of tensile and compressive demand, locate vulnerable panels and compare alternative interventions under identical earthquake inputs. The physical meaning of local stress extrema must nevertheless be assessed together with damage contours and displacement response.

Sib Castle, in southeastern Iran, includes a perimeter enclosure and a two-story central residence. Its thick earthen walls, stepped geometry and discontinuous roofs form interacting lateral-load paths. The assessment brings together the monument's material tests, a three-dimensional masonry macro-model, a wall-scale experimental benchmark and three pairs of recorded ground motions. Two locally applied CFRP patterns were designed around the structural hotspots rather than imposed over the entire monument.

The objectives were to identify seismic demand concentrations, establish the response of the unstraightened castle, compare grid and diagonal 1.0-mm CFRP strip layouts, and interpret their effects on both global deformation and local stress demand. The comparison is explicitly a comparison of two specified reinforcement schemes, not a material-efficiency test at equal bonded area.

The article first reviews relevant adobe and FRP research, then describes the castle, constitutive modelling, numerical verification and earthquake inputs. The response and strengthening results are followed by a mechanistic discussion of their significance for conservation engineering.

2. Literature Review and Research Gap

Mirjalili et al. (2020) tested 12 adobe wall panels under cyclic lateral loading. The variables included three height-to-width ratios and four vertical pre-compression levels (0.1–0.7 MPa). Their results showed that strength, stiffness and the prevailing failure mechanism depend strongly on geometry and axial stress. This provides a suitable experimental basis for the present wall-scale benchmark, which adopts a 0.5 MPa reference state. The wall test does not capture the varied restraints and wall-to-roof connections of the complete fortress.

Eslami et al. (2021) examined in-plane cyclic response of adobe wall panels strengthened by near-surface-mounted steel bars, GFRP bars and reeds. Their tests showed that near-surface-mounted reinforcement improved in-plane performance, with steel bars providing the strongest response among the materials examined. Abdulla et al. (2021) studied hemp-rope reinforcement for out-of-plane adobe wall response and demonstrated a different, low-mass strengthening mechanism. Neither experiment is directly interchangeable with the externally bonded, full-scale CFRP arrangement examined here: the loading mode, interface and scale differ.

Castellazzi et al. (2017) demonstrated the importance of survey-informed geometry in finite-element assessment of monumental masonry. Their work supports the decision to retain openings, irregular wall intersections and vertical setbacks in the Sib Castle model instead of simplifying the monument into regular blocks. Such geometric fidelity helps explain why high tensile demand recurs at specific architectural discontinuities.

FRP performance depends not only on material stiffness but also on strip placement and bond transfer. Petrovčič and Kilar (2022) evaluated six FRP layouts in a three-story historic masonry building and considered performance together with reinforcement quantity. Ghiassi et al. (2013) demonstrated that water exposure can weaken FRP-to-masonry bonding, while Vaculik et al. (2018) identified limitations of existing bond-test interpretations. Together, these findings support comparing the layouts separately from the bond performance that might be achieved on site.

The study relates local CFRP placement to the earthquake response of a surveyed, irregular three-dimensional adobe monument. The work adds a directional comparison of two specific retrofit patterns to a field in which evidence is frequently obtained from isolated wall specimens or simplified masonry buildings. The proposed configurations are assessed as conservation-oriented numerical interventions rather than universally optimal reinforcement details.

3. Sib Castle and Material Characterization

3.1. Geometry and Structural Configuration

The original architectural survey documents the surviving earthen wall system, changes in wall thickness and openings that govern structural connectivity. Because conservation history can be unevenly recorded, the assessment focuses on the documented geometry and modelled structural components rather than inferring undocumented past interventions (Fakouri-Nejad, 2025).

Sib (Seb) Castle is located in the village of Sib in the Sistan and Baluchestan Province of southeastern Iran, near Saravan. The settlement lies in a hot, dry, semi-mountainous region, and the castle is founded on a rocky base. The primary structural material is sun-dried adobe laid in earthen mortar. The traditional flat roof is formed by timber or palm-trunk members supporting secondary vegetal layers and earthen topping.

The complex can be divided into three principal components: the perimeter enclosure, rooms arranged around the enclosure, and the central governor's residence. The enclosure is approximately 74 m × 48 m. The governor's section is approximately 36 m × 25 m and develops over two principal levels. The central courtyard, multiple openings, stepped elevations, and changes in wall thickness create a highly irregular three-dimensional load path. These features are important because they alter the distribution of seismic inertia forces and introduce stress concentrations that cannot be represented adequately by an idealized rectangular block.

The castle is a long-standing earthen monument whose historical fabric reflects successive periods of use and maintenance. Because the structural assessment does not depend on assigning a specific construction dynasty, the present study focuses on the documented geometry, materials, and current structural configuration (Fakouri-Nejad, 2025).

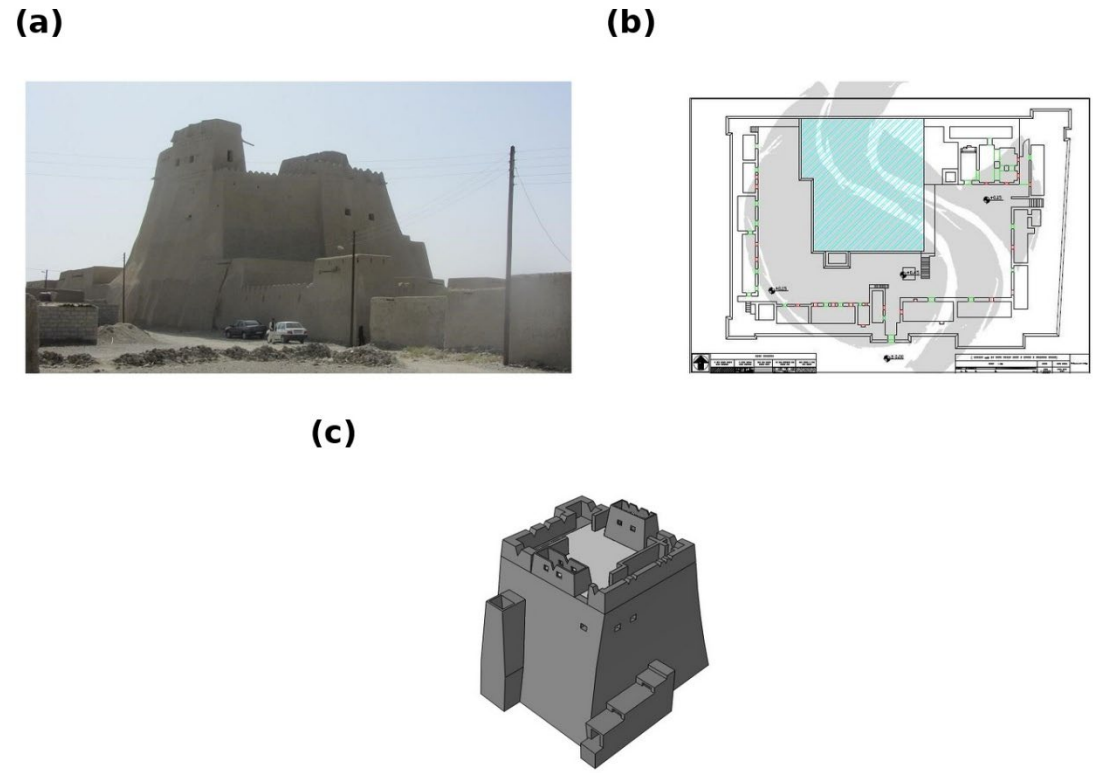


Figure 1. Sib Castle and numerical reconstruction: (a) north elevation, (b) ground-floor architectural plan, and (c) three-dimensional finite-element geometry

3.2. Survey and Material Tests

The site documentation includes both a village-scale location map and architectural drawings of the perimeter enclosure and governor's residence. These records were used to preserve the real plan irregularity, openings, wall intersections, and changes in elevation during the AutoCAD reconstruction.

Material characterization was based on original adobe and earthen-mortar specimens taken from representative parts of the monument. The specimens were documented photographically before testing and used to establish the mechanical properties of the equivalent masonry continuum.

Table 1. Compression test results for earthen specimens from Sib Castle

ID	Material	L×W×H (cm)	Density (g/cm³)	Failure load (kgf)	fc (kgf/cm²)
A1	Adobe	16.8×12.8×5.9	1.74	8300	39
A2	Adobe	15.3×11×5.5	1.73	7000	42
A3	Adobe	13.6×9.8×5.0	1.70	5500	41
S1	Straw-adobe	6.2×5.4×4.5	1.70	1500	45
S2	Straw-adobe	5.8×5.2×4.2	1.69	1300	43
S3	Straw-adobe	6.5×5.6×3.6	1.71	1480	41

Compression tests on the supplied earthen specimens reported strengths of 39–42 kgf/cm² for adobe and 41–45 kgf/cm² for straw-adobe. These unit strengths should not be substituted directly for the effective masonry-continuum strength. The underlying thesis distinguishes specimen results from an equivalent masonry material model (Fakouri-Nejad, 2025).

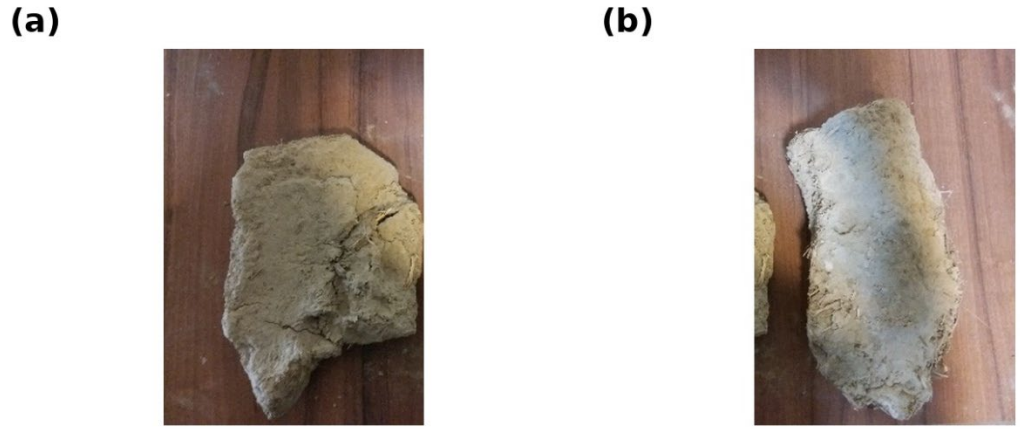


Figure 2. Representative fractured earthen specimens after compression testing; the measured strengths are summarized in Table 1

3.3. Equivalent Masonry Properties

Original adobe and earthen-mortar samples from representative parts of Sib Castle were compression-tested to establish the material basis of the macro-model. The adobe specimens developed compressive strengths of 39–42 kgf/cm² and the straw-adobe specimens 41–45 kgf/cm². The equivalent masonry strength used in the global model was then obtained from the adobe/mortar homogenization procedure documented in the underlying research, rather than by assigning the unit strength directly to the continuum.

For the equivalent masonry continuum, the adopted compressive strength was approximately 1.94 MPa and the tensile strength was taken as 10% of this value, approximately 0.194 MPa. The elastic modulus was evaluated from E = 550 f_m, giving approximately 1067 MPa; Poisson's ratio was 0.20 and density was approximately 1850 kg/m³. These properties were

used consistently in the castle analyses and provide the reference tensile threshold against which the principal tensile-demand maps are interpreted (Fakouri-Nejad, 2025).

Table 2. Equivalent masonry properties adopted in the three-dimensional model

Parameter	Value	Parameter basis
Density	≈ 1850 kg/m³	Equivalent continuum
Equivalent compressive strength	≈ 1.94 MPa	Unit/mortar strength homogenization
Tensile strength	≈ 0.194 MPa	10% of compressive strength
Elastic modulus	≈ 1067 MPa	E = 550 fm
Poisson ratio	0.20	Macro-model assumption

4. Nonlinear Finite-Element Model

4.1. Geometry and Macro-Modelling

The numerical geometry followed the architectural survey rather than an idealized block. Existing architectural plans, elevations, and survey information were first reviewed and redrawn in AutoCAD. The perimeter walls, internal rooms, governor's residence, principal openings, level differences, and major thickness changes were retained. This stage served as a geometry-control step and allowed inconsistencies in the available drawings to be identified before finite-element discretization (Castellazzi et al., 2017; Fakouri-Nejad, 2025).

The AutoCAD reconstruction was used as the geometric reference rather than as the final analytical model. The geometry was subsequently rebuilt or transferred into Abaqus/CAE and partitioned into meshable three-dimensional solids. Decorative details without structural significance and redundant geometric entities were removed to improve numerical robustness, but the major discontinuities that influence seismic behavior particularly openings, corners, wall intersections and vertical setbacks were preserved.

A macro-modelling strategy was adopted for the earthen walls. Individual adobe units and mortar joints were not represented explicitly; instead, the masonry assemblage was treated as a homogenized continuum with equivalent mechanical properties. This choice reduced the number of degrees of freedom sufficiently to make nonlinear bidirectional response-history analysis of the entire fortress computationally feasible while still allowing global stress redistribution and damage localization to be examined (Castellazzi et al., 2017; Fakouri-Nejad, 2025).

The compact architectural figure condenses the geometric information used for modelling: the ground-floor plan defines the perimeter and internal walls, the governor's-residence plan captures the central irregularity, and the finite-element view shows how these features were carried into the three-dimensional Abaqus model.

4.2. Constitutive Modelling of Earthen Masonry

The masonry response was described by the Abaqus Concrete Damaged Plasticity (CDP) model. The adopted flow-potential parameters were dilation angle $\psi = 15°$, eccentricity $\varepsilon = 0.10$, biaxial-to-uniaxial yield-stress ratio $f_{b0}/f_{c0} = 1.16$, deviatoric shape parameter $K_c = 0.66$ and viscosity coefficient $\mu = 0.0$. Inelastic compression, tension softening and the associated damage evolution were specified by the material curves used in the underlying numerical study (Fakouri-Nejad, 2025).

CDP was selected as a homogeneous continuum approximation of adobe masonry, not as a claim that adobe and ordinary concrete share identical micromechanics. Its practical advantage is the ability to represent tensile degradation and compressive nonlinearity within a large three-dimensional model. Local damage and peak stress should be interpreted at the resolution of the adopted mesh: a continuum cannot resolve individual joints or the exact separation path of a discrete adobe crack.

The CDP material definition includes tensile softening, compressive hardening and their corresponding tensile and compressive damage evolution. These tabulated constitutive branches govern the redistribution of stress after cracking in the masonry macro-model. Because strain-softening localizes deformation, the damage contours are interpreted together with the geometry and mesh resolution rather than as direct measurements of individual crack widths. The numerical formulation thereby provides a consistent means of comparing the selected earthquake and CFRP scenarios.

4.3. Timber Roofs

The traditional timber–earth roof was represented with orthotropic timber properties based on the underlying structural study. The adopted density was 680 kg/m³. Elastic moduli were $E_1 = 864$ MPa, $E_2 = 1956$ MPa and $E_3 = 12{,}000$ MPa; the corresponding shear moduli were $G_{12} = 420$ MPa, $G_{13} = 936$ MPa and $G_{23} = 1032$ MPa. The orientation of these constants followed the local material axes used for the roof representation.

4.4. Elements and Boundary Conditions

The castle was discretized predominantly using four-node linear tetrahedral solids (C3D4); timber and the separate wall benchmark were represented with the element formulations described in the thesis. The C3D4 element provides constant strain within each tetrahedron. Gravity loading, fixed-foundation constraints and the two-horizontal ground-acceleration inputs were applied in the same numerical framework for the comparative castle analyses.

At wall scale, the thesis compared characteristic mesh sizes of 20 and 25 mm and selected 20 mm after observing closely corresponding principal-stress patterns. This comparison informed

the local benchmark discretization. The more complex castle model used C3D4 elements to follow irregular openings and intersections, where local stress gradients are intrinsically more sensitive to geometric detail than global modal quantities.

4.5. Numerical Model Verification

The reference wall measured 1.0 × 0.9 × 0.20 m and comprised adobe units approximately 200 × 200 × 45 mm in size. In the experimental programme, a sustained axial force of 100 kN produced an average vertical stress of 0.50 MPa over the 1.0 × 0.20 m section. In the Abaqus/Explicit benchmark, the equivalent adobe continuum was represented with C3D8R solids and subjected to displacement-controlled lateral loading to 15 mm. The first loading branch of the experimental cyclic response was compared with the numerical pushover curve (Mirjalili et al., 2020; Fakouri-Nejad, 2025).

The integrated experimental and numerical response-envelope areas were 678.7 and 668.2, respectively. Relative to the experimental area, the difference was $|678.7 - 668.2|/678.7 \times 100 = 1.55\%$. This integrated comparison indicates close agreement in the selected response branch. It should not be interpreted as equal agreement in every ordinate, nor as a measure of cyclic energy dissipation, because only the initial loading branch of the laboratory response was used.

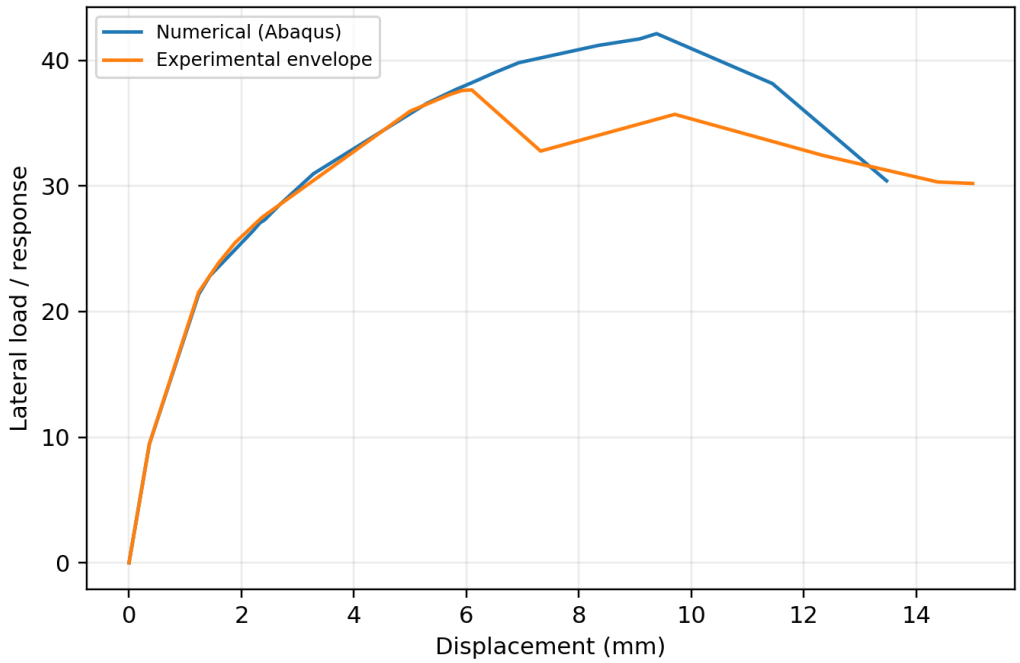


Figure 3. Experimental and numerical lateral response of the reference adobe wall

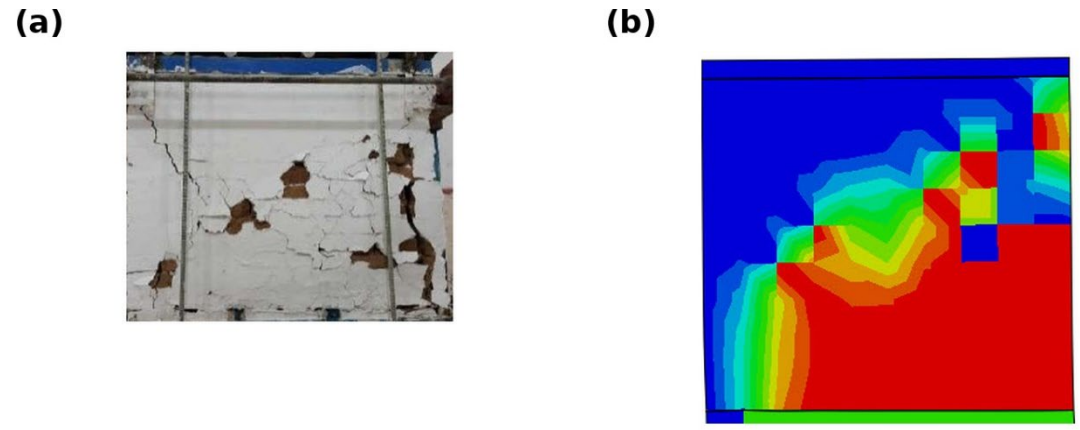


Figure 4. Validation of the failure mechanism: experimental diagonal cracking and corresponding numerical damage localization

The experimental wall developed a diagonal cracking mechanism, and the numerical damage field showed a corresponding diagonal concentration. The agreement is important because it links lateral resistance to a plausible shear-tension mechanism rather than matching an aggregate curve alone. The benchmark establishes confidence in the wall-scale mechanism and force–displacement response under the selected axial stress; it does not imply that discrete mortar-joint slip is directly represented by the homogeneous CDP formulation.

4.5.1. Interpretation of Wall Verification

The comparison is deliberately made on the first in-plane loading branch. Subsequent laboratory reversals involve crack closing, unloading stiffness, pinching and cumulative damage, whereas the numerical benchmark follows a monotonic push. The 1.55% area difference and the consistent diagonal-crack direction are therefore complementary wall-scale checks, not a calibration of the full hysteretic response.

Figure 4 juxtaposes the experimental damage photograph with the numerical damage pattern. Damage concentrated diagonally across the panel rather than spreading uniformly over its surface. Such qualitative agreement is especially relevant for the castle, where intersecting walls and openings likewise produce localized tension paths. The comparison remains mechanistic because the continuum model does not track the opening width of individual adobe joints.

4.6. Mesh Sensitivity and Numerical Reliability

The wall mesh study in the thesis compared 20- and 25-mm characteristic element sizes. Their principal-stress distributions were close, and 20 mm was selected for the wall benchmark. This is a useful check on the broad stress pattern, but in strain-softening masonry the highest local stress may vary with element size, particularly near corners and geometric constraints.

The full castle differs from the benchmark wall in both geometry and element formulation. In the castle, local concentration near re-entrant corners, window edges and wall–roof intersections is governed by the three-dimensional mesh and by the strain-softening law. Accordingly, the evaluation here emphasizes recurring critical regions, story-relative displacement and integrated base reaction rather than treating a single extreme contour value as a mesh-independent material property.

Global response and local damage do not have the same sensitivity to discretization. Natural frequencies and overall displacement reflect integrated mass and stiffness; concentrated tensile fields depend more strongly on the discretization of openings, intersections and weakened zones. The two types of response are therefore interpreted separately in the seismic discussion.

4.7. Influence of Material Parameters

The mechanical parameters influence different aspects of the calculated response. Masonry elastic modulus controls initial period and stiffness; tensile strength and softening regulate crack initiation and redistribution; dilation and compressive parameters influence shear resistance. For CFRP shells, the governing membrane stiffness in the fibre direction scales with E1t, where t is the modelled thickness. This distinction is essential when comparing laminate data expressed for an impregnated thickness with data expressed per fibre-equivalent thickness.

In explicit analysis, a smoothly applied gravity step helps restrain unintended inertial effects before earthquake excitation. CDP tensile softening can localize within a narrow region, making the computed damage contour sensitive to element size. These well-known modelling features explain why the present comparisons rely on several complementary measures stress, damage pattern and deformation rather than peak stress alone.

5. Dynamic Assessment and Ground-Motion Selection

5.1. Analysis Stages and Response Metrics

Table 3. Numerical analysis sequence and principal response metrics

Stage	Primary input	Response metrics	Engineering purpose
Modal analysis	Mass and stiffness	Natural frequencies, T1	Characterize dynamic behavior
Gravity analysis	Self-weight	Stress, damage, displacement	Establish baseline response
Nonlinear response history	Two components of three records	Stress/damage, displacement, drift, base shear	Identify critical record and critical regions
CFRP retrofit	Critical Tabas case + two layouts	Stress and deformation	Compare the two specified CFRP layouts

5.1.1. Definition of Comparison Measures

Five response measures guide the comparisons: percentage reduction of a specified stress or displacement metric, the ratio of computed stress demand to nominal tensile strength, story-relative displacement, normalized story drift where story height is known, and CFRP membrane stiffness per unit width. Their definitions are given below.

$$\eta\sigma = 100 \times (\sigma u - \sigma s)/\sigma u. \quad (1)$$

$$Rt = \sigma max / ft. \quad (2)$$

$$\theta i = (ui - ui{-}1)/hi. \quad (3)$$

$$\Delta A = 100 \times |Aexp - Anum|/Aexp. \quad (4)$$

$$Kf = E1\ t. \quad (5)$$

Here η denotes the reduction in the same response measure relative to the unstraightened state. The quantity Rt is an elastic-demand reference and not a CDP damage index. Where the thesis reports a 'drift' in centimeters, the quantity is described as story-relative displacement; a dimensionless drift ratio requires division by the corresponding story height. The axial-stiffness product E1t is used only to compare materials defined on compatible thickness bases.

5.2. Modal Characteristics

Modal analysis gave the first two natural frequencies as 4.5647 and 4.7851 Hz. The corresponding fundamental period was T1 = 1/4.5647 = 0.2191 s. Response spectra were evaluated at 5% damping. The dynamic model used the Rayleigh coefficients reported in the source analysis, $\alpha \approx 2.73\ s^{-1}$ and $\beta \approx 9.12 \times 10^{-4}$ s (Fakouri-Nejad, 2025). As stiffness degrades after cracking, these initial modal properties no longer describe the complete response history.

Table 4. First ten natural frequencies of the Sib Castle model

Mode	Frequency (Hz)
1	4.5647
2	4.7851
3	6.3954
4	9.5201
5	10.271
6	10.590
7	10.923
8	11.123
9	11.726
10	11.978

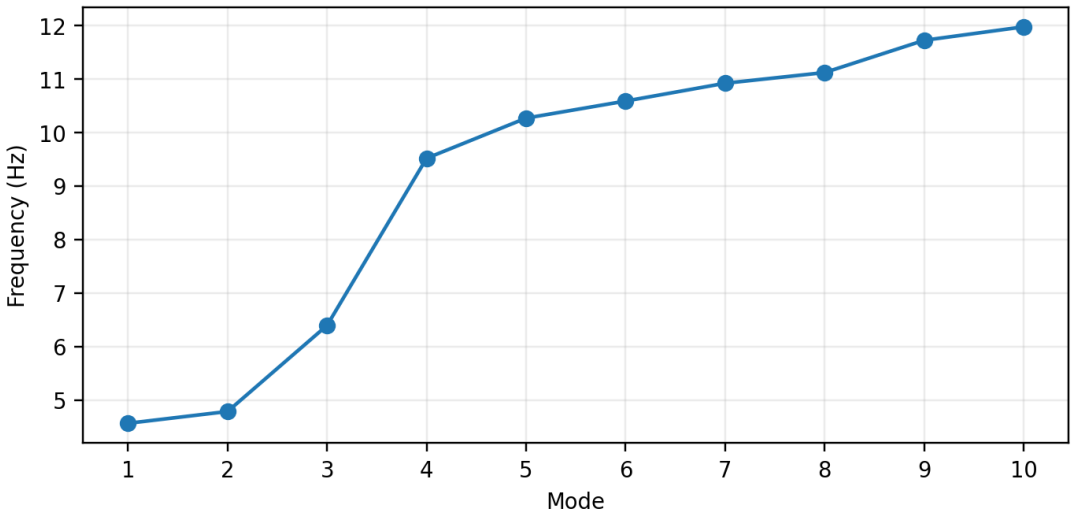


Figure 5. First ten natural frequencies of the numerical model

5.3. Gravity Response

The self-weight analysis showed localized tensile demand near roof junctions, the upper edges of walls and abrupt level changes. Compressive stresses remained below the adopted equivalent compressive strength of the masonry. This suggests that gravity-driven vulnerability was linked more closely to tensile discontinuity and inter-component compatibility than to global compressive crushing. These regions also provided useful reference locations for evaluating earthquake-induced damage.

The short initial period places the elastic response within a range where record-specific spectral ordinates can vary substantially. Once tensile cracking reduces effective stiffness, the dynamic characteristics evolve, and the relative ordering of maximum force and maximum displacement may differ across earthquake inputs. This is pertinent when interpreting the larger Tabas deformation alongside the larger Sarpol-e Zahab base shear.

5.4. Record Selection and Spectral Scaling

Three pairs of horizontal accelerograms were considered: Tabas (1978, M 7.8), Kobe (1995, M 6.9) and Sarpol-e Zahab (2017, M 7.3). Table 5 gives the sampling interval, duration, two horizontal PGAs and amplitude scale factors reported in the numerical study. These records were chosen to compare distinct acceleration histories and spectral characteristics, not to establish statistical seismic hazard (Fakouri-Nejad, 2025).

The response spectra were assessed at 5% damping and the pairs were amplitude-scaled according to the procedure adopted from Iranian Standard 2800. With $T1 \approx 0.2191$ s, the target period interval 0.2T1–1.5T1 was 0.0438–0.3287 s. The scaling method used the mean SRSS spectrum of the two horizontal components from each pair. The factors listed in Table 5 were

subsequently applied to both components of the respective records; scaling is distinguished from waveform-modifying spectral matching.

Table 5. Ground-motion descriptors and spectral amplitude factors used in the analyses

Record / M / reported site velocity (m/s)	Δt (s)	Duration (s)	Original PGA, H1/H2 (g)	SF1	Total SF	Scaled PGA, H1/H2 (g)
Tabas 1978 / 7.8 / 377.56	0.020	38.98	0.091 / 0.067	11.1111	5.4363	0.495 / 0.364
Kobe 1995 / 6.9 / 609	0.010	53.99	0.092 / 0.110	10.0000	4.8926	0.450 / 0.538
Sarpol-e Zahab 2017 / 7.3 / 481.2	0.005	99.445	0.686 / 0.563	1.6667	0.8154	0.559 / 0.459

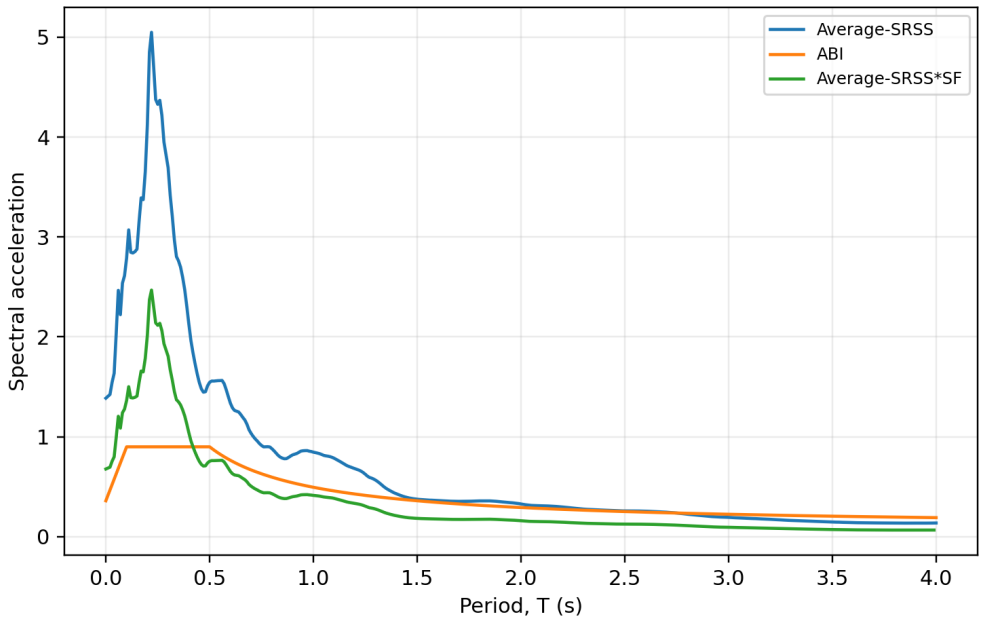


Figure 6. Response-spectrum scaling: average SRSS spectrum, target code spectrum, and scaled spectrum

5.5. Ground-Motion Processing, Component Synchronization and Spectral Scaling

The horizontal acceleration histories were prepared for spectral evaluation using SeismoSignal, as described in the thesis. Their original time increments and durations are presented in Table 5. The analyzed PGA values in the same table follow from the record amplitudes and reported total scale factors; the time axis remains unchanged by multiplicative amplitude scaling.

Both horizontal components of a record form a single ground-motion pair. They were used as simultaneous X- and Z-direction inputs, preserving the time relationship within that pair. Synchronizing the component sampling is important because maximum bidirectional action

depends on the phase and duration of the complete traces, not merely on the separate component peaks.

The selected motion pairs were normalized, their 5%-damped component spectra were calculated, and the two horizontal spectral ordinates were combined by SRSS. The mean SRSS response of the three pairs was then compared with the Standard 2800 design spectrum over 0.2T1–1.5T1. The tabulated total scale factors are 5.4363 (Tabas), 4.8926 (Kobe) and 0.8154 (Sarpol-e Zahab). The same pair-specific factor was applied to both horizontal components, maintaining the relative component amplitudes.

The three pairs provide a controlled comparison of the model response to distinct earthquake inputs. Record-to-record differences should be interpreted in terms of spectral shape, temporal sequence and nonlinear stiffness evolution. Three pairs are not a probabilistic sample from which a general collapse risk or fragility relationship can be inferred.

6. Seismic Response of the Unstraightened Castle

The unstraightened castle developed maximum-principal tensile-stress values of approximately 5.26 MPa under Tabas, 4.01 MPa under Kobe and 2.60 MPa under Sarpol-e Zahab. These are maxima of the reported finite-element stress field. They describe localized model demand and should not be divided by the nominal masonry tensile strength (0.194 MPa) to infer a proportional measure of physical damage. Crack development is interpreted alongside the tensile-damage fields and the associated structural deformation.

Despite differences in amplitude, the three inputs produced recurring tensile-demand concentrations at opening corners, external walls, intersections between internal and external walls, and roof-level discontinuities. This spatial consistency indicates that geometry and load-path discontinuities largely determine where cracks are likely to initiate. The input motion governs the severity and temporal progression of the response. The damage contours also point to tension as a more significant mechanism than compressive crushing for the analyzed cases.

Table 6. Maximum principal tensile-stress metrics for the unstraightened castle

Record	Peak principal tensile stress (MPa)	Interpretation
Tabas	≈ 5.26	Largest local tensile-stress metric
Kobe	≈ 4.01	Second-largest local tensile-stress metric
Sarpol-e Zahab	≈ 2.60	Lowest of three local tensile-stress maxima

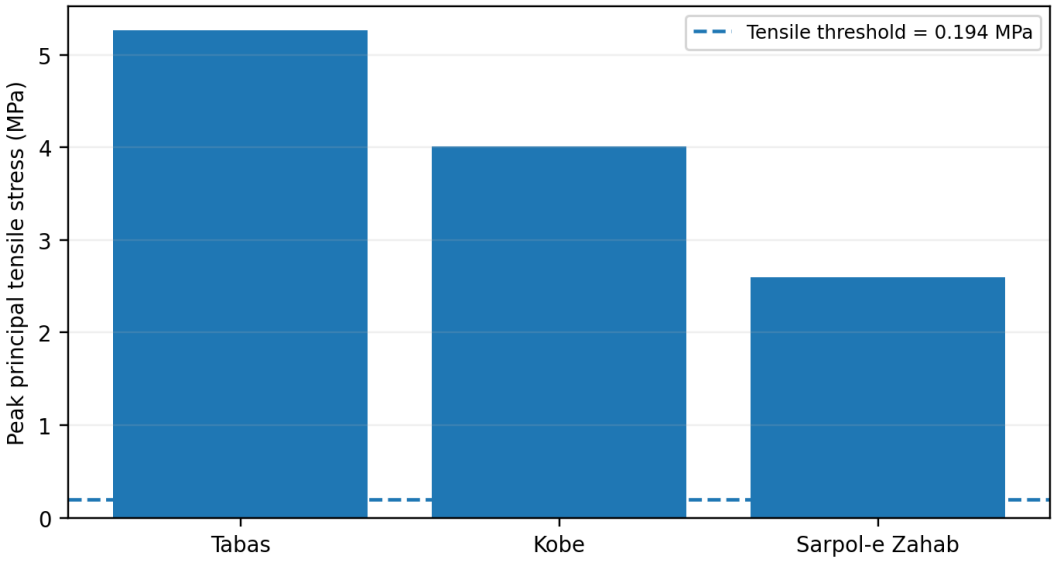


Figure 7. Peak principal tensile stress for the three earthquake records compared with the adopted masonry tensile strength

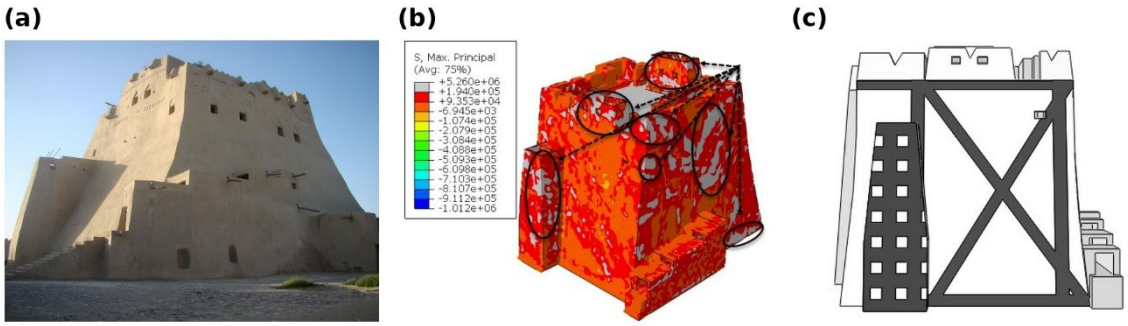


Figure 8. Damage-driven selective CFRP strengthening concept: (a) real façade geometry containing openings and upper-wall interfaces associated with numerical vulnerability; (b) high tensile-demand zones in the unstraightened model under the critical Tabas record; and (c) a representative local CFRP layout applied only to the critical wall panel rather than to the entire castle surface

A second intervention example concerns the opening-rich upper wall region. The field photograph shows the actual façade, while the numerical field identifies the corresponding type of tensile hotspot. The strengthening sketches then illustrate the two alternatives: an orthogonal grid that crosses opening-adjacent tension paths in multiple directions and diagonal strips that follow selected diagonal crack trajectories.

Figure 9 connects the geometric source of vulnerability to the predicted damage pathway. The highlighted crack-prone directions are schematic interpretations of the numerical result rather than a survey of existing cracks. In this way, the images communicate both the rationale for the selected reinforcement locations and the distinction between a calculated hotspot and observed deterioration.

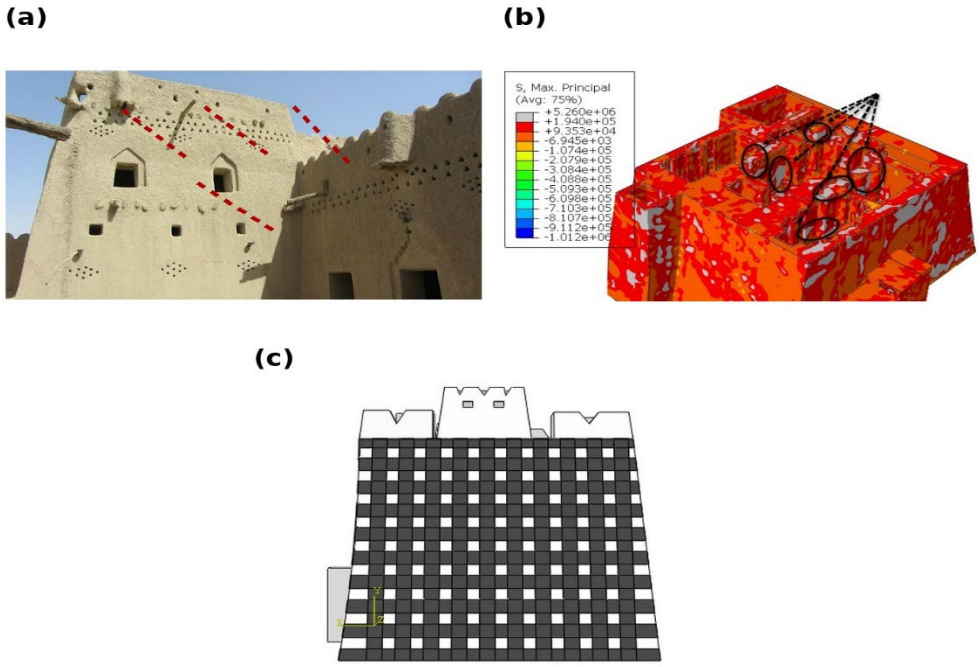


Figure 9. Linking the real monument to the numerical prediction and local strengthening concept: (a) real façade geometry with numerically inferred crack-prone paths highlighted schematically; (b) Abaqus tensile-damage / hotspot pattern for the corresponding vulnerable wall zone; and (c) a local CAE-based strengthening concept showing selective CFRP placement on the critical region only

6.1. Story-Relative Displacements

For the unstraightened castle, the first-story X-direction relative displacement was 22.0 cm under Tabas, compared with 1.5 cm under Kobe and 0.6 cm under Sarpol-e Zahab (Table 7). The corresponding Z-direction values were 0.09, 0.27 and 0.20 cm. These are displacement quantities in centimeters, not dimensionless drift ratios. The pronounced X-direction Tabas response identifies the governing deformation case for the retrofit comparison.

The record ordering changes when a different response indicator is considered. Different spectra can excite the structure near different evolving modes; once masonry cracks, the effective stiffness and internal force distribution also change. Hence the event producing the greatest lateral displacement need not produce the greatest base reaction. The results are consistent with this mechanical distinction, without treating earthquake magnitude as a direct predictor of castle response.

Table 7. Story-relative displacements under the three earthquake records (cm)

Record	Story 1, X (cm)	Story 1, Z (cm)	Story 2, X (cm)	Story 2, Z (cm)
Tabas	22.0	0.09	3.8	0.20
Kobe	1.5	0.27	1.1	0.36
Sarpol-e Zahab	0.6	0.20	0.3	0.13

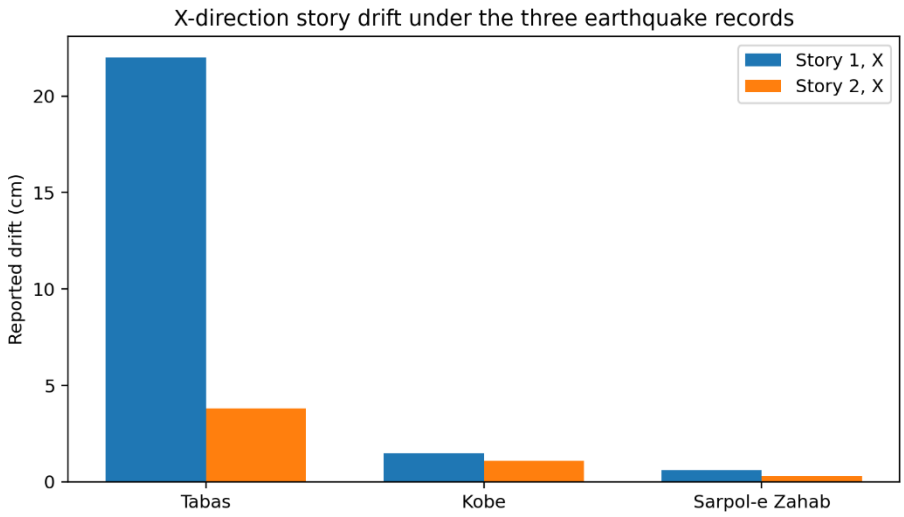


Figure 10. X-direction story-relative displacements under the three earthquake records

6.2. Base Shear

The Sarpol-e Zahab input generated the largest reported base-shear demand in the X and Z directions, whereas Tabas governed the displacement and tensile-demand comparisons. Base shear reflects the integrated inertial and reaction response of the structure, while large deformation can develop after local stiffness loss. The two observations are complementary rather than contradictory.

For an earthen monument, a high base-reaction peak may occur before extensive cracking. Conversely, a lower reaction level can accompany larger relative displacement when parts of the masonry have softened. A seismic diagnosis should therefore combine base-shear ranking with the locations of tensile damage and with the displacement pattern across the monument.

7. CFRP Strengthening and Comparative Assessment

7.1. Strengthening Concept

Only carbon-fiber-reinforced polymer (CFRP) was implemented in the numerical retrofit model. Accordingly, the strengthening discussion is restricted to the CFRP system actually analyzed. The retrofit layout was defined only after the unstraightened nonlinear analyses had identified the dominant tensile-demand zones of the castle.

7.2. CFRP Material and Idealized Interface

The retrofit was modelled using orthotropic CFRP shell strips with a nominal thickness of 1.0 mm. The material parameters used in the study include longitudinal elastic modulus E1 = 181 GPa, transverse modulus E2 = 10.3 GPa, Poisson's ratio v12 = 0.28 and shear moduli G12 = G13 = 7.17 GPa and G23 = 3.58 GPa. These parameters define the generic lamina adopted in

the numerical investigation; no claim is made that a particular commercial SikaWrap product was directly modelled.

The strips were attached to the masonry surface using an Abaqus Tie constraint. The constraint imposes displacement compatibility across the interface, allowing a controlled comparison of the two layouts under the same idealized bond condition. It does not represent the local opening or sliding of the adhesive interface, peeling of the adobe substrate or end-anchor failure. The implication for conservation practice is discussed separately from the numerical response comparison.

Two arrangements were examined in the selected wall regions: an orthogonal grid and a diagonal-cross layout. The grid provides horizontal and vertical bridging paths around openings and at wall intersections; diagonal strips directly cross selected inclined tensile paths. Both interventions were concentrated at the critical external walls and upper-level junctions identified by the baseline analyses.

The comparison isolates the response of two practical reinforcement patterns under the same structural model and earthquake input. Their coverage and reinforcement length are not necessarily identical. A better response from one pattern therefore indicates improved performance of that specific configuration, not intrinsic superiority of its fibre direction at equal material consumption.

7.2.1. Interface Limitations

The perfect-bond representation is an analytical boundary condition, not a prediction of adhesive strength. Experiments on FRP–masonry joints show that the bond is sensitive to material condition, testing arrangement and moisture exposure (Ghiassi et al., 2013; Vaculik et al., 2018). In adobe, a weak near-surface layer may govern before the composite reaches its tensile resistance. This affects implementation details even when the global FE response is favorable.

A heritage intervention must also address visual intrusion, compatibility with earthen plaster, moisture migration, inspection access and potential removal. These requirements do not alter the comparative numerical results, but they determine whether an externally bonded solution can be justified for a specific wall panel (ICOMOS, 2003; Petrovčič & Kilar, 2022).

Table 8. Adopted CFRP lamina properties and interface assumptions

Parameter	Value	Model status
E1	181 GPa	Adopted longitudinal modulus
E2	10.3 GPa	Transverse modulus
ν12	0.28	Major Poisson ratio
G12 = G13	7.17 GPa	In-plane / longitudinal shear
G23	3.58 GPa	Transverse shear
Xt = Xc	1500 MPa	Longitudinal tensile/compressive strengths
Yt	40 MPa	Transverse tensile strength
Yc	246 MPa	Transverse compressive strength
SL	96 MPa	Longitudinal shear strength
ST	48 MPa	Transverse shear strength
Hashin α	0	Damage-initiation parameter
Shell thickness	1.0 mm	Author-confirmed reference thickness
Interface	Tie constraint	Perfect-bond baseline

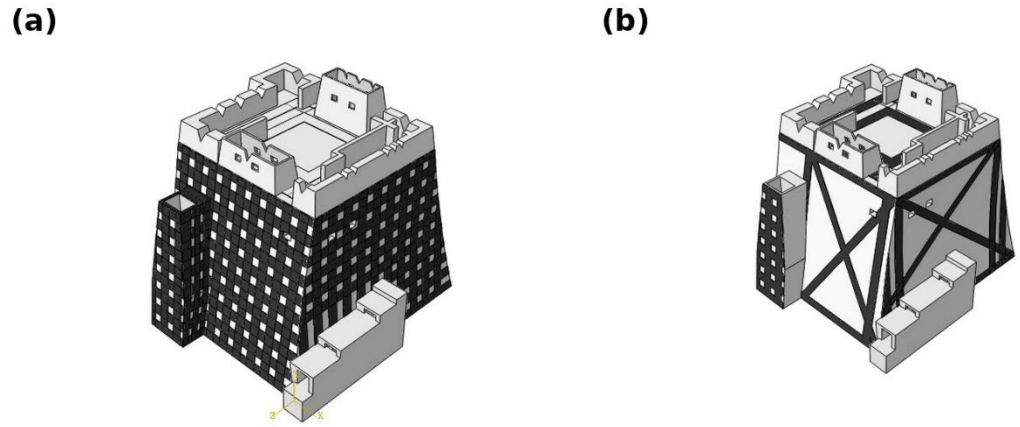


Figure 11. CFRP strengthening layouts evaluated numerically: grid/checkerboard and diagonal/cross configurations

7.2.2. Physical Laminate Properties Versus Equivalent-Fiber Data

SikaWrap-230 C with Sikadur-330 provides a useful illustration of why reinforcement thickness must be defined consistently. Its 2006 data sheet reports a typical impregnated laminate thickness of 1.0 mm and modulus of 28 GPa, equivalent to an axial tensile stiffness of approximately 28 MN/m per unit width. A newer product specification refers the modulus of approximately 225 GPa to a fiber-equivalent thickness of 0.129 mm, giving approximately 29 MN/m. The two descriptions are physically consistent in membrane stiffness but do not imply identical flexural properties (Sika, 2006; Sika, n.d.).

The present numerical CFRP uses a different, generic orthotropic lamina. At its adopted thickness of 1.0 mm, E1t = 181 MN/m, substantially larger than the illustrative SikaWrap product-basis values. The results should therefore be interpreted for the specified numerical

material rather than transferred directly to a named commercial product. In classical shell theory, axial stiffness scales as E1t while bending stiffness varies approximately with E1t³; the distinction matters when a fiber-only and a saturated-laminate convention are compared.

The nominal 1.0-mm shell-section thickness is used consistently in the description of both strengthening configurations. The CFRP arrangements differ in strip placement and fiber path, while the orthotropic constitutive law and the idealized connection remain the same. The study does not use a product-specific impregnation or adhesive constitutive model.

Table 9. CFRP modelling properties compared with SikaWrap-230 C product-basis data

Property	Adopted orthotropic CFRP	Sika (2006) impregnated	Sika recent fiber-equivalent
E1 (GPa)	181	28	225
E2 (GPa)	10.3	Not specified	Not specified
G12 (GPa)	7.17	Not specified	Not specified
G13 (GPa)	7.17	Not specified	Not specified
G23 (GPa)	3.58	Not specified	Not specified
ν12	0.28	Not specified	Not specified
Thickness (mm)	1.0 (author-confirmed)	1.0 saturated	0.129 fiber-equivalent
Plies	Equivalent shell lamina	One composite layer	One fabric layer
E1t (MN/m)	181	28	29.025

7.2.3. Response Metrics and Comparison Basis

The two retrofitted models were assessed using the same baseline structural representation and Taba's excitation. Peak principal tensile stress and story-relative displacement provide complementary response measures: the first traces maximum local demand, and the second shows how a reinforcement arrangement changes global deformation. The calculated stress reduction is defined relative to the corresponding unstraightened peak and is not interpreted as a direct percentage reduction in physical crack length or collapse probability.

A numerical comparison of reinforcement efficiency must also distinguish performance from material quantity. The grid contains more intersecting strips and potentially greater bonded coverage than a diagonal scheme. Accordingly, the following results establish the relative effectiveness of the two modelled layouts, while conservation-related material efficiency remains tied to the footprint of the selected intervention.

7.3. Strengthening Zones and Patterns

The unstraightened analyses identified tensile hotspots at upper wall edges, near roof connections, at wall intersections and around openings. These are the locations where force transmission changes abruptly and where limited earthen tensile capacity is likely to trigger

local cracking. CFRP was therefore placed along selected external wall regions and upper-level interfaces rather than applied uniformly across the castle.

The orthogonal grid bridges several possible crack trajectories across a given wall panel and provides a more continuous reinforcing path around openings. The diagonal arrangement is directed toward inclined tensile fields and leaves a smaller fraction of the surface covered. The first configuration was more effective for the governing X-direction displacement, whereas the second retained a lower intervention footprint in the illustrated layouts.

The proposed design sequence begins with nonlinear diagnosis, followed by targeted treatment of the recurrent critical regions. Figures 8 and 9 relate the real geometry to the numerical tensile-demand map and illustrate the consequent reinforcement placement. This avoids equating a large total reinforcement area with good conservation practice; any intervention is justified by a particular structural deficiency.

7.4. Comparison of Response

The unstraightened, grid-strengthened and diagonally strengthened models were compared under the Tabas excitation. The geometry, nominal masonry properties, ground-motion input and idealized interface assumption were held common to the model comparison. The quantities below therefore measure the influence of the two specified CFRP layouts on the computed response.

The peak principal tensile-stress metric decreased from 5.26 MPa without CFRP to 0.191 MPa for the grid and 0.193 MPa for the diagonal scheme (Table 10). With the unstraightened peak as denominator, the arithmetic reductions were 96.37% and 96.33%, respectively. Their difference is small: 0.002 MPa, or about 1.0% of the diagonal value. The result supports the effectiveness of CFRP in redistributing this numerical stress demand, but the near-equal peak values do not, on their own, establish a substantial grid advantage.

Deformation provides a clearer distinction between the layouts. The first-story X-direction relative displacement decreased from 22 cm to 5 cm for the grid (77.27%) and to 19 cm for the diagonal scheme (13.64%). The second-story X-direction values decreased from 3.8 cm to 1.8 and 2.5 cm, respectively. In contrast, the second-story Z-direction values increased from 0.20 cm to 1.30 cm for the grid and 0.70 cm for the diagonal configuration. This directional trade-off matters: neither arrangement can be described as reducing all story-relative displacements. The full comparison is given in Table 11 (Fakouri-Nejad, 2025, Table 4-7).

Table 10. Maximum principal tensile-stress metric under Tabas

Model	Peak tensile-stress metric (MPa)	Stress reduction (%)
Unstraightened	≈ 5.26	Reference
Grid/checkerboard CFRP	≈ 0.191	96.37
Diagonal/cross CFRP	≈ 0.193	96.33

The near-equality of the two strengthened stress maxima in Table 10 does not predict the same deformation response. Table 11 therefore compares the four story- and direction-specific relative displacements. The larger X-direction benefit of the grid must be considered alongside the increased second-story Z-direction values.

Table 11. Tabas-induced story-relative displacements before and after CFRP strengthening (cm)

Configuration	Story 1 X	Story 1 Z	Story 2 X	Story 2 Z
Unstraightened	22.0	0.09	3.8	0.20
Grid CFRP	5.0	0.06	1.8	1.30
Diagonal CFRP	19.0	0.07	2.5	0.70

The CFRP strips reached reported peak stresses of 81.3 MPa in the grid layout and 183 MPa in the diagonal arrangement (Fakouri-Nejad, 2025, Table 4-6). The lower strip stress in the grid is consistent with load being distributed across a larger number of reinforcement paths, although differences in strip quantity must also be considered. It does not establish bond adequacy, which is outside the Tie interface formulation.

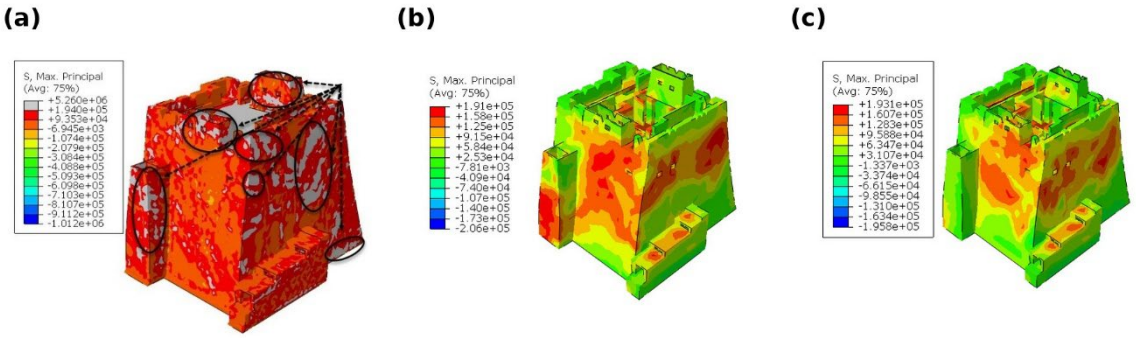


Figure 12. Maximum principal tensile-stress metrics for the unstraightened and CFRP-retrofitted models under Tabas

8. Discussion and Comparison with Previous Studies

The principal finding is that tensile demand repeatedly concentrates around openings, wall intersections and roof-level discontinuities. These regions have interrupted force-transfer paths and limited capacity to redistribute tension after cracking. Their identification agrees with the geometry-sensitive response of monumental masonry discussed by Castellazzi et al. (2017). The present study extends this reasoning to an irregular earthen fortress analyzed under bidirectional nonlinear earthquake excitation.

The records did not govern the same response quantities. Tabas produced the largest X-direction story-relative displacement and the highest reported local tensile-stress metric, whereas Sarpol-e Zahab produced the largest base-shear response. Peak displacement and base reaction need not coincide in a nonlinear structure, particularly when cracking changes its effective stiffness. In their cyclic adobe-wall tests, Mirjalili et al. (2020) likewise considered strength, stiffness degradation and displacement capacity as distinct descriptors of response.

The benchmark wall showed a diagonal failure pattern and a 1.55% difference in the selected envelope-area comparison. The agreement supports the adopted macro-model for the wall-scale in-plane mechanism. It is narrower than full cyclic validation, because laboratory loading reversals introduce crack closure, residual displacement and energy dissipation. The distinction is relevant to heritage engineering: the most defensible extrapolation from the wall benchmark is the location and progression of tensile cracking, not a fully calibrated hysteretic collapse prediction.

The two CFRP layouts gave similar reductions in the reported local tensile-stress maxima but rather different deformation responses. For the first story under Tabas, the grid reduced X-direction relative displacement by 77.27%, while the diagonal layout achieved 13.64%. The grid spans several possible crack paths and connects more of the vulnerable wall network; the diagonal arrangement is more closely tied to the assumed orientation of principal tension. Petrovčič and Kilar (2022) also found that the distribution and amount of FRP affect building-scale response. Their nonlinear-static masonry case is not a direct quantitative analogue of the present dynamic adobe model.

The change in Z-direction response prevents an indiscriminate conclusion that the grid is superior in every respect. In the second story, the reported Z-direction relative displacement increased in both strengthened models, especially in the grid case. The local increase may reflect redistribution of stiffness and deformation between connected walls; the analysis establishes the change in response but not a unique causal mechanism. The increased transverse response therefore matters as much as the reduction in the governing X-direction response.

The CFRP stress response adds another dimension. Maximum strip stresses in the thesis were approximately 81.3 MPa for the grid and 183 MPa for the diagonal pattern under Tabas. The

diagonal scheme therefore developed about 2.25 times the peak CFRP stress of the grid in the specific models. Relative to the nominal longitudinal lamina strength of 1500 MPa, the corresponding ratios are approximately 5.4% and 12.2%; these are material stress ratios under idealized bonding and do not measure the likelihood of adobe peeling or adhesive debonding.

8.1. Findings in Relation to Adobe-Wall Experiments

Adobe-wall experiments provide a useful mechanism-level comparison, not a direct quantitative retrofit benchmark. Mirjalili et al. (2020) found that axial compression and aspect ratio influence in-plane cyclic cracking and strength. Eslami et al. (2021) showed the benefits of near-surface-mounted reinforcement in adobe panels, while Abdulla et al. (2021) demonstrated a different out-of-plane strengthening mechanism using hemp ropes. The present fortress model combines wall interaction, openings and bidirectional input, so percentage changes in these distinct tests should not be equated without matching geometry, load paths and interface conditions.

The selected CFRP areas in Sib Castle follow a recurring field of numerical tensile demand rather than the wall-wide treatment used in many component tests. This distinction is useful for heritage protection: a high-performing wall detail is not automatically the most appropriate intervention when multiple walls and roofs interact, or when substantial coverage would obscure the historic surface.

8.2. Interface Behavior and Conservation Compatibility

The Abaqus Tie constraint transmitted load without interface slip, separation or substrate peeling. Its purpose was to compare global layouts under a common, idealized bond law. The sensitivity of composite–masonry bond to moisture documented by Ghiassi et al. (2013), and the range of bond-test interpretations reviewed by Vaculik et al. (2018), show why numerical strain compatibility should not be confused with an experimentally established adobe bond capacity.

This distinction is particularly important for weak historic earthen finishes. Adhesive penetration, near-surface cohesion, moisture exchange and the possibility of removal can determine whether the intervention is acceptable even when the global response improves. ICOMOS (2003) and Valluzzi et al. (2014) support a design process that balances structural gains with minimal disturbance and material compatibility.

8.3. Comparison with Building-Scale FRP Retrofits

Petrovčič and Kilar (2022) examined six FRP configurations in a historic three-story masonry building and included material quantity in the evaluation. Their work demonstrates that improving the global response and limiting the extent of strengthening are related but distinct

objectives. In Sib Castle, the grid substantially reduced the governing X-direction displacement, while the diagonal scheme used a less extensive illustrated pattern. Without imposing equal area, these are comparative outcomes of two specific layouts rather than an optimization of strength gained per unit reinforcement.

The modest difference between grid and diagonal peak tensile-stress values contrasts with their much larger difference in the X-direction displacement response. This suggests that the spatial continuity of the reinforcement and its interaction with the wall network influence deformation more strongly than a single local stress extreme reveals. The second-story Z-direction increase reinforces the need to examine response along both horizontal axes.

8.4. Engineering Significance and Methodological Scope

The study combines the surveyed geometry of an irregular earthen fortress with a wall-scale CDP benchmark, three bidirectional earthquakes and two local CFRP arrangements. Unlike an isolated wall test, the global model permits the interaction of openings, wall intersections and floor-level changes to influence intervention placement. The repeated hotspot locations across the three motions are therefore more useful for conservation decisions than any one peak contour color.

These findings must be read in the context of the adopted modelling assumptions. A homogeneous masonry continuum captures structural-scale redistribution but not the detailed mechanics of individual adobe joints. Similarly, perfect CFRP bond provides a consistent basis for comparing layouts but excludes local connection failure. The three-record set describes three specified seismic scenarios; its results are not a probabilistic estimate of site risk.

A conservation-compatible scheme must consequently consider the entire chain of performance: the location of weak walls, the directional response of the monument, the amount of historical surface treated and the compatibility of the adhesive with the substrate. The reported X-direction benefit of the grid is compelling within the adopted model, but an increase in another response component remains a design consideration rather than a result to be concealed.

8.5. Implications for Intervention Planning

The model is most useful for locating weaknesses and comparing interventions. Reinforcement should be directed to the recurring critical walls and opening interfaces, with the extent of intervention determined by structural need and conservation constraints. The grid configuration is a promising candidate where controlling the Tabas-governed X-direction deformation is paramount. The diagonal layout remains an alternative where the pattern can follow a clear tension path and reduced surface coverage carries greater architectural value.

Both layouts should be evaluated with a site-specific substrate and bonding strategy before physical implementation. The response improvement belongs to the numerical layouts studied; practical detailing must also address the bond and condition of the historic substrate.

The central finding is therefore not that any application of CFRP improves every measure. Rather, targeted orthotropic strips can markedly reduce the governing model response, and the size and direction of that improvement depend on reinforcement geometry and the response measure selected.

9. Conclusions

A three-dimensional nonlinear finite-element study of Sib Castle identified the dominant seismic vulnerability of its adobe structure and compared two local 1.0-mm CFRP reinforcement layouts. The following conclusions are supported by the wall-scale benchmark, the three seismic analyses and the reported comparative results:

1. The adobe macro-model employed CDP with $\psi = 15°$, $\varepsilon = 0.10$, $f_{b0}/f_{c0} = 1.16$, $K_c = 0.66$ and $\mu = 0.0$. Tensile damage was concentrated around openings, wall intersections and upper wall–roof discontinuities, where geometric irregularity interrupts the load path.

2. The wall-scale model reproduced the characteristic diagonal failure path. The integrated numerical and experimental force–displacement envelope areas differed by 1.55%, using the experimental area as denominator. This benchmark supports the selected in-plane mechanism while remaining distinct from a complete cyclic hysteresis calibration.

3. The first elastic frequency was 4.5647 Hz ($T_1 = 0.2191$ s). Among the three bidirectional motions, Tabas governed the reported peak tensile-demand and X-direction relative displacement, whereas Sarpol-e Zahab produced the larger integrated base-shear response.

4. Under Tabas, the reported maximum-principal tensile-stress metric decreased from 5.26 MPa to 0.191 MPa with the grid and 0.193 MPa with the diagonal arrangement. The corresponding arithmetic reductions were 96.37% and 96.33%. These values quantify changes in the computed stress metric rather than a proportional change in physical damage or collapse probability.

5. The first-story X-direction relative displacement was reduced from 22 cm to 5 cm for the grid (77.27%) and to 19 cm for the diagonal scheme (13.64%). Both arrangements also reduced the second-story X-direction response, but increased the second-story Z-direction displacement. Consequently, retrofit efficiency is direction- and metric-dependent.

6. The grid developed a lower peak strip stress than the diagonal layout (81.3 versus 183 MPa) and was more effective in limiting the governing X-direction deformation. This performance

applies to the two modelled layouts and should not be read as a comparison at equal reinforcement quantity.

7. Selective CFRP placement provides a plausible conservation-oriented means of reducing predicted seismic demand without blanket coverage of the monument. The numerical comparison uses idealized CFRP–adobe bonding; substrate compatibility, moisture response, anchorage and reversibility remain essential considerations for intervention design.

Conflict of interest. Disclosure of potential competing interests is provided by the authors through the journal submission process.

Acknowledgements. The authors acknowledge the experimental study of Mirjalili et al. (2020), which provided the reference adobe-wall response used for numerical benchmarking.

10. References

Abdulla, K. F., Cunningham, L. S., & Gillie, M. (2021). Out-of-plane strengthening of adobe masonry using hemp fiber ropes: An experimental investigation. Engineering Structures, 245, 112931. https://doi.org/10.1016/j.engstruct.2021.112931

Castellazzi, G., D'Altri, A. M., de Miranda, S., & Ubertini, F. (2017). An innovative numerical modeling strategy for the structural analysis of historical monumental buildings. Engineering Structures, 132, 229–248. https://doi.org/10.1016/j.engstruct.2016.11.032

Dassault Systèmes. (n.d.). Abaqus analysis user's guide: Concrete damaged plasticity. SIMULIA.

Eslami, A., Zahedi, A., & Mirabi Banadaki, H. (2021). In-plane seismic behavior of NSM strengthened adobe walls: Experimental evaluation of different reinforcements. Engineering Structures, 246, 113016. https://doi.org/10.1016/j.engstruct.2021.113016

Fakouri-Nejad, A. (2025). Seismic analysis of Sib Castle, Saravan, and strengthening using FRP [Master's thesis, Islamic Azad University, Zahedan Branch]. [In Persian].

Ghiassi, B., Marcari, G., Oliveira, D. V., & Lourenço, P. B. (2013). Water degrading effects on the bond behavior in FRP-strengthened masonry. Composites Part B: Engineering, 54, 11–19. https://doi.org/10.1016/j.compositesb.2013.04.074

International Council on Monuments and Sites (ICOMOS). (2003). Principles for the analysis, conservation and structural restoration of architectural heritage. https://www.icomos.org/images/DOCUMENTS/Charters/structures_e.pdf

Mirjalili, A., Eslami, A., & Morshed, R. (2020). Experimental investigation into the effect of vertical loading on in-plane cyclic behavior of adobe walls. Construction and Building Materials, 264, 120706. https://doi.org/10.1016/j.conbuildmat.2020.120706

Petrovčič, S., & Kilar, V. (2022). Design considerations for retrofitting of historic masonry structures with externally bonded FRP systems. International Journal of Architectural Heritage, 16(7), 957–976. https://doi.org/10.1080/15583058.2020.1853278

Road, Housing and Urban Development Research Center. (2014). Iranian code of practice for seismic resistant design of buildings (Standard No. 2800, 4th ed.).

Sika. (2006, June 13). SikaWrap-230 C: Woven carbon fiber fabric for structural strengthening [Product data sheet]. https://www.petrolinetech.com/wp-content/uploads/2021/12/SikaWrap-230-C.pdf

Sika. (n.d.). SikaWrap®-230 C: Product data. https://aus.sika.com/en/construction/structural-strengthening/shear-strengthening/sikawrap-230-c.html

Vaculik, J., Visintin, P., Burton, N. G., Griffith, M. C., & Seracino, R. (2018). State-of-the-art review and future research directions for FRP-to-masonry bond research: Test methods and techniques for extraction of bond-slip behavior. Construction and Building Materials, 183, 325–345. https://doi.org/10.1016/j.conbuildmat.2018.06.103

Valluzzi, M. R., Modena, C., & de Felice, G. (2014). Current practice and open issues in strengthening historical buildings with composites. Materials and Structures, 47, 1971–1985. https://doi.org/10.1617/s11527-014-0359-7